A Multi-Contact, Low Capacitance HPGe Detector for High Rate Gamma Spectroscopy

Topic	23a
Company Name	XIA LLC
Company Address	31057 Genstar Rd, Hayward, CA 94544
Principal Investigator	Christopher Cox
Grant Award Number	DE-SC0011354
Report Number	DOE-XIA-11354

Phase I Final Technical Report

12/04/2014

Executive Summary

The detection, identification and non-destructive assay of special nuclear materials and nuclear fission by-products are critically important activities in support of nuclear non-proliferation programs. Both national and international nuclear safeguard agencies recognize that current accounting methods for spent nuclear fuel are inadequate from a safeguards perspective. Radiation detection and analysis by gamma-ray spectroscopy is a key tool in this field, but no instrument exists that can deliver the required performance (energy resolution and detection sensitivity) in the presence of very high background count rates encountered in the nuclear safeguards arena. The work of this project addresses this critical need by developing a unique gamma-ray detector based on high purity germanium that has the previously unachievable property of operating in the 1 million counts-per-second range while achieving state-of-the-art energy resolution necessary to identify and analyze the isotopes of interest.

The technical approach was to design and fabricate a germanium detector with multiple segmented electrodes coupled to multi-channel high rate spectroscopy electronics. Dividing the germanium detector's signal electrode into smaller sections offers two advantages; firstly, the energy resolution of the detector is potentially improved, and secondly, the detector is able to operate at higher count rates. The design challenges included the following; determining the optimum electrode configuration to meet the stringent energy resolution and count rate requirements; determining the electronic noise (and therefore energy resolution) of the completed system after multiple signals are recombined; designing the germanium crystal housing and vacuum cryostat; and customizing electronics to perform the signal recombination function in real time.

In this phase I work, commercial off-the-shelf electrostatic modeling software was used to develop the segmented germanium crystal geometry, which underwent several iterations before an optimal electrode configuration was found. The model was tested and validated against real-world measurements with existing germanium detectors. Extensive modeling of electronic noise was conducted using established formulae, and real-world measurements were performed on candidate front-end electronic components. This initial work proved the feasibility of the design with respect to expected high count rate and energy resolution performance. Phase I also delivered the mechanical design of the detector housing and vacuum cryostat to be built in Phase II. Finally, a Monte Carlo simulation was created to show the response of the complete design to a Cs-137 source.

This development presents a significant advance for nuclear safeguards instrumentation with increased speed and accuracy of detection and identification of special nuclear materials. Other significant applications are foreseen for a gamma-ray detector that delivers high energy resolution (1keV FWHM noise) at high count rate (1 Mcps), especially in the areas of physics research and materials analysis.

Contents

	Page
1. Introduction	3
2. Phase I Technical Objectives.	3
3. Task 1: HPGe crystal design.	3
4. Task 2: Validation of capacitance and electric field models.	8
5. Task 3: Detector noise model, and sources of excess noise.	10
6. Task 4: Crystal housing and cryostat design.	17
7. Task 5: Response to a ^{137}Cs source.	19
8. Task 6: Reporting.	20
9. Summary	20
10. References	20

1. Introduction

The following report describes the results and accomplishments of the multi-contact, low-capacitance HPGe detector Phase I work plan, with particular emphasis on how the Phase I Technical Objectives have been met. The numeration of the Technical Objectives and Tasks corresponds to that in the Phase I proposal.

1.1 Definitions

Throughout the report, the following terms have the specific definitions described below:

HPGe crystal refers to the germanium material fabricated with segmented electrodes into a working device. HPGe detector is the working crystal housed in the cryostat assembly with front-end electronics and preamplifiers.
HPGe detector system refers to the completed HPGe detector running with the XIA multi-channel electronics.
Electrode, signal electrode, and contact are synonymous.

2. Phase I Technical Objectives

The long term technical objective of the project is to design, develop and commercialize a high-rate and high-resolution HPGe detector system based on the HPGe crystal design concept of multiple low-capacitance contacts. The following Phase I Technical Objectives were established to demonstrate the feasibility of the technical approach:

1. HPGe crystal design: Determine the optimal contact configuration, size, location and number to satisfy the design requirements of contact capacitance and charge collection time.
2. Validate the model of the segmented HPGe crystal used to achieve Technical Objective 1.
3. Characterize the expected noise performance of the designed HPGe detector at short peaking times.
4. Identify contact fabrication issues that will be addressed in Phase II.
5. Determine the design of the final detector assembly to be fabricated in Phase II, including mounting of the HPGe crystals, electrical connections, and the liquid nitrogen vacuum cryostat housing.
6. Determine the response of the final detector assembly to a ^{137}Cs source to quantify the collection efficiency at 662 keV.
7. Write reports, possibly publications and Phase II proposal.

To accomplish the Technical Objectives, the work plan was subdivided into the Phase I Tasks described below. Results and accomplishments for each Task are reported under the appropriate headings.

3. Task 1: HPGe Crystal Design

The purpose of Task 1 was to determine the HPGe crystal size and contact configuration by modeling the capacitance and the worst and best-case drift times for each electrode, iterating the design, changing the size, number and location of electrodes to optimize the configuration in terms of capacitance and charge collection time. The resulting design was required to meet the specification of <5pF for all signal electrodes, and worst-case charge collection times of <200ns.

It was determined that three other design considerations must be taken into account, in addition to the capacitance and charge collection time at each electrode. Firstly, the volume of the detector must be sufficient to offer reasonable collection efficiency in the energy range of interest. For the purposes of this work, that can be determined by estimating the full-energy absorption of 662 keV gamma rays from ^{137}Cs. (Task 5 determines the quantitative response to ^{137}Cs). Secondly, the charge from a single gamma-ray event should arrive at all electrodes simultaneously to within 200 ns. For example, a design that produces fast signal rise times by relying on high electric field regions only near the signal electrodes, but with weaker fields elsewhere, may not be suitable for high rate work due to the spread (~μs) in the charge arrival times at the different electrodes, thereby increasing the effective dead-time for each event. Thirdly, there is a secondary noise effect associated with the

number of electrodes employed in the design, specifically the sharing of charge from a single gamma-ray event. The XIA multi-channel signal processing electronics will be used to sum time-coincident events from multiple electrodes to generate the full incident energy, but there are consequences for the electronic noise. For example, if charge is shared between two electrodes that generate electronic noise N eV FWHM each, then the noise component of the summed signal is √2.N. There is therefore a noise advantage in selecting a detector design where the charges produced by a typical incident gamma-ray interact with as few signal electrodes as possible.

3.1 Task 1 Accomplishments

3.1.1. Physical dimensions and electrode structure.

When considering the HPGE crystal design, it was necessary to prioritize the conflicting requirements of low capacitance, charge collection efficiency, charge collection time, and the number of contacts. To this end, the following order of priority was chosen to guide the design;

1) Electric field strength, which places fundamental constraints on the maximum size of the HPGe crystal.
2) Collection efficiency at 662 keV.
3) Contact capacitance.
4) Number of contacts.

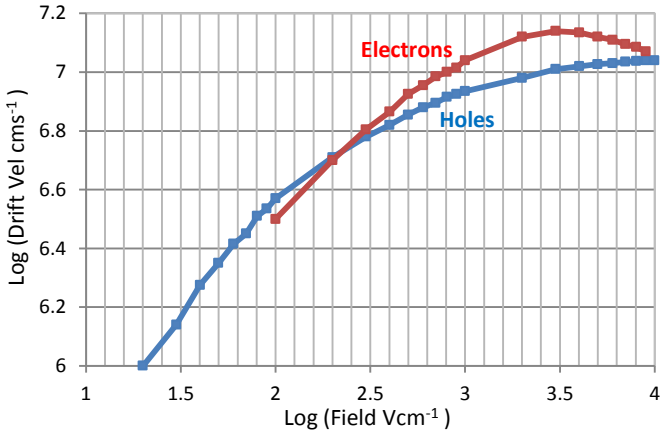

Figure 1. Log-Log plot of Drift Velocity vs. Electric Field for holes [1] and electrons [2] at 77 K.

In consideration of the electric field strength (priority #1), it was decided that a planar crystal structure offered the best field strength throughout the volume of the detector, with the worst-case charge collection time being fundamentally limited by the thickness of the crystal. In the ideal case of a true HPGe planar crystal with full-area electrodes operating at a few kV high voltage, the electric field is typically in the range of 1-2 $kVcm^{-1}$, (depending on the net carrier concentration of the germanium material), which produces electron and hole drift velocities of about 10^7 cms^{-1}, (figure 1). In this ideal case, the worst-case charge drift time for a 15 mm thick crystal is 150 ns, somewhat faster than the specification of 200 ns. 15 mm was therefore chosen as the crystal thickness, in anticipation that modeling with segmented electrode designs would likely produce weaker field regions and potentially longer charge drift times.

The detector design uses two back-to-back 15 mm thick planar HPGe crystals to improve the collection efficiency (stopping power) for 662 keV gamma rays, (priority #2). The response to a ^{137}Cs source will be reported in detail in Task 5, but as a check on the initial design concept a simple linear calculation gives about 70% absorption in 30 mm of germanium at 662 keV. Although the field strength is independent of the crystal diameter (to a first order), a dimension of 40 mm diameter was chosen based on initial capacitance calculations, and the desire to keep each electrode capacitance below 5pF. Since the XIA electronics will combine all coincident electrode signals, for charge collection purposes the two crystals can be considered as one unit with dimensions 40 mm diameter x 30 mm thickness. Note that these are typical dimensions for a small coaxial HPGe gamma detector.

With the overall crystal dimensions established, the design was developed by modeling various electrode configurations and sizes, at each stage checking electrode capacitances, electric field strengths and estimated charge drift times. In keeping with priorities above, the goal was to determine the minimum number of contacts with <5pF capacitance that met the charge collection criteria. For capacitance and electric field modeling we used the commercially available software packages "Electro" (2D) and "Coulomb" (3D) from Integrated Engineering Software. The software allowed the determination of the E_x, E_y, E_z electric field components along the x, y, and z axes at any point on a plane cross section through the crystal. Another feature of the software was

the ability to add a fixed charge density in the body of the crystal to simulate the germanium net carrier concentration; this is a necessary feature to correctly simulate electric fields in germanium.

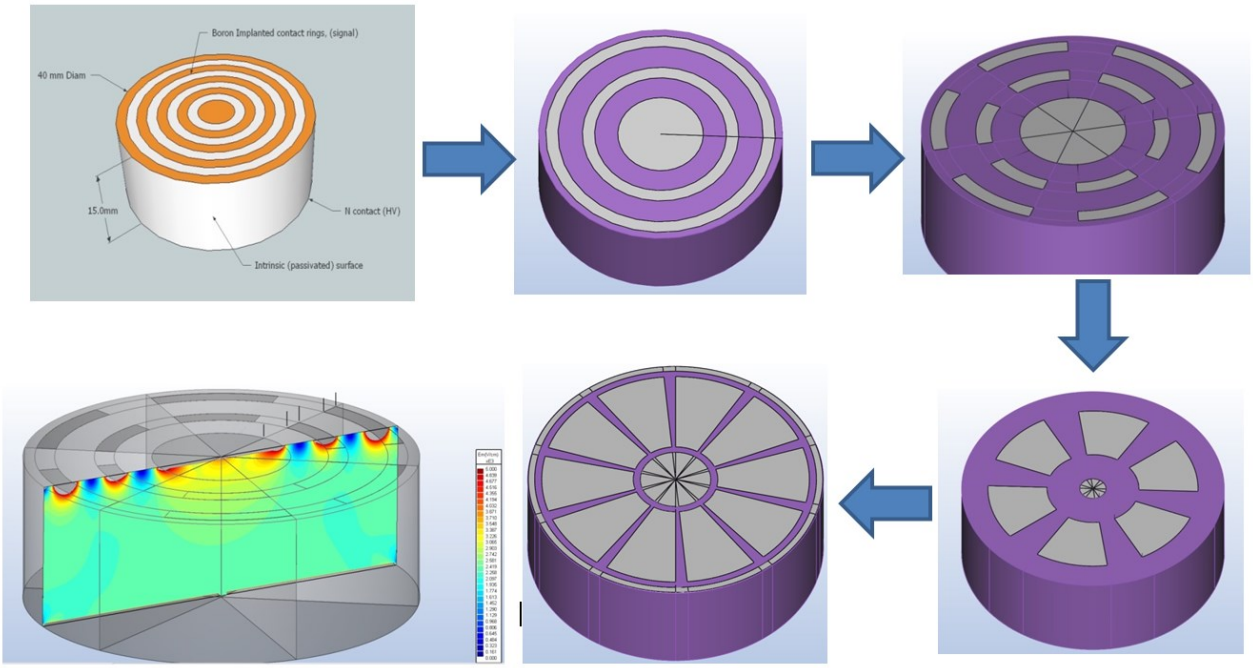

Figure 2. Evolution of the HPGe crystal design, with sample electric field plot from an early segmented ringed design.

Figure 2 shows the evolution of the design resulting from the considerations mentioned above. In each case the model assumes the crystal is fabricated from p-type germanium with a lithium diffused full-area n^+ high voltage contact on the rear of the crystal, (not visible in figure 2), and p^+ boron ion implanted segmented contacts on the opposite face. The area down the sides of the crystal and between the segmented electrodes is treated with a passivation process to control the surface charge and reduce leakage current. Note that in the case of a planar detector the gamma-ray interaction point is likely to occur anywhere within the crystal volume, and the resulting signal is generated by holes and electronics with roughly equal probability. Therefore, the usual argument for using n-type material to avoid neutron damage does not apply here, as either polarity material will be equally susceptible to hole traps.

During the design phase, worst-case charge drift times were calculated by transforming the modeled electric field into the electron and hole drift velocities using the data in figure 1, and then integrating the charge transit time in small increments (0.01 mm) along the (weak field) path of interest. Using this method, an early part of the study investigated the ringed structure and the effect on capacitance and charge transit time of the ring width, the gap between the rings, the number of rings, and segmenting the rings into smaller sections. The initial conclusions were firstly that the charge collection model seemed to tolerate quite a large ring gap, up to several mm, and secondly it was necessary to segment the rings (and unfortunately increase the number of electrodes) to reduce capacitance to an acceptable level, inter-segment capacitance being a particular problem.

With further investigation, it was found that a design with near-trapezoidal electrodes was more efficient in covering the surface of the crystal for the same capacitance, and gave slightly improved charge collection; this was the next step in the evolution of the design. Furthermore, after discussions with the proposed detector manufacturer, Canberra, we understood that the passivated area between the segmented electrodes is very difficult to control and cannot be modeled satisfactorily due to the buildup of surface charge during the fabrication process. Therefore, in order to avoid unexpected weak and/or distorted fields in the electrode gap areas we were advised to keep the electrode gap in the 1 to 1.5 mm range. The resulting final design is shown in figures 2 and 3, and features a circular center electrode, ten near-trapezoid electrodes with small gap spacing, and an outer guard-ring to reduce field distortions (and potential weak fields) down the sides of the crystal. The

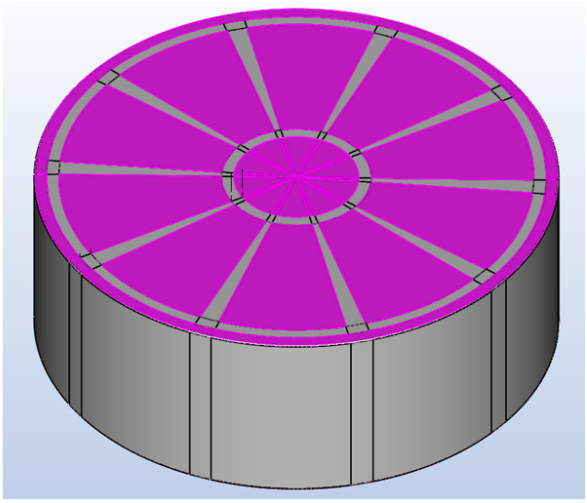

Dimensions	
Crystal diameter	42 mm
Crystal thickness	15 mm
Crystal corner radius	0.1 mm
Center electrode diameter	10 mm
Length of trapezoidal segment	13 mm
Angle subtended by trapezoidal segment	31^0
Guard ring width	1 mm
Width of passivated gap between segments	1-1.5 mm
Total active volume of germanium (2 crystals)	36 cm^3

Total Capacitances	
Center electrode to ground	4.47 pF
Trapezoidal electrode to ground	4.66 pF

Fig. 3. Schematic of the final crystal design with dimensions and electrode capacitances. The magenta areas represent the ion implanted segmented electrodes. The full-area lithium diffused HV contact is on the underside of the crystal and not visible in the schematic. The gray areas represent passivated intrinsic germanium surfaces. (The black lines on the schematic are a product of the CAD software and have no significance.)

crystal dimensions are given in figure 3. Figure 3 also shows the total capacitances to ground for both electrode types, which include the effect of all inter-electrode capacitances. It should be noted that the guard ring introduces a 1mm thick dead-layer around the sides of the crystal which potential reduces the gamma ray collection efficiency slightly. However, 1 mm of germanium still permits 96% transmission at 662 keV, so the guard ring dead layer is not a concern for the target application. In principal, the diameter could be increased with no effect on the field strength, but this would result in a larger number of electrodes in order to meet the capacitance requirement of each.

3.1.2. Electric field models and charge drift time.

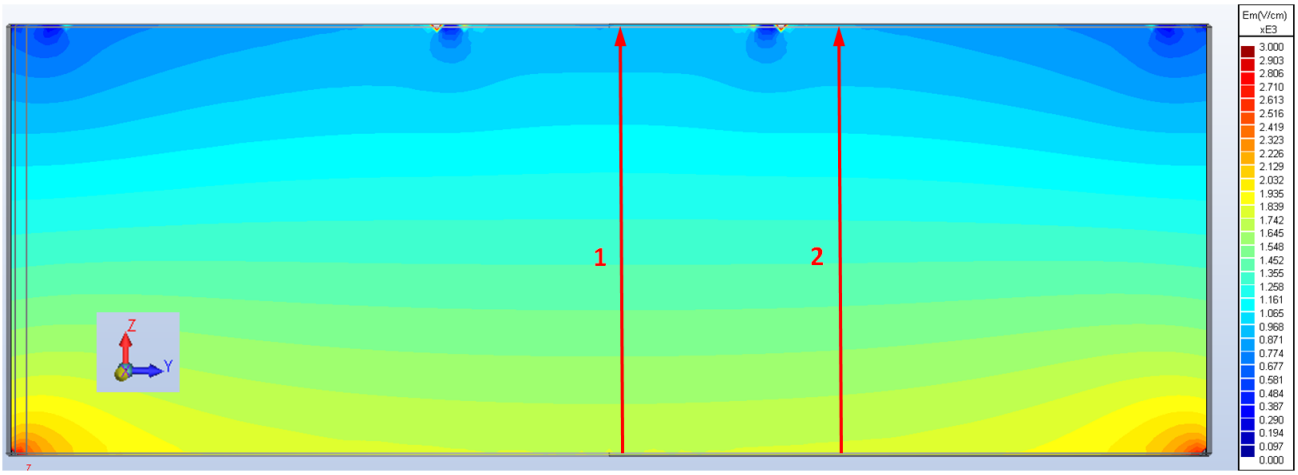

Fig 4. Cross section of the HPGe crystal through the trapezoidal segment area showing the electric field contours. The lines labeled 1 and 2 refer to the Ez field component plots in fig 7.

Figure 4 is a plot of the total electric field through a plane cross section of the final crystal design, bisecting two of the trapezoidal electrodes. The actual electric field strength in a working detector will depend, of course, on the germanium material net carrier concentration and the crystal operating bias. In our model we have assumed a typical net carrier concentration of $1x10^{10}$ cm^{-3}, and a modest HV bias of -2000V. In practice, the actual operating bias may be somewhat higher, depending on the leakage current, thereby increasing the field

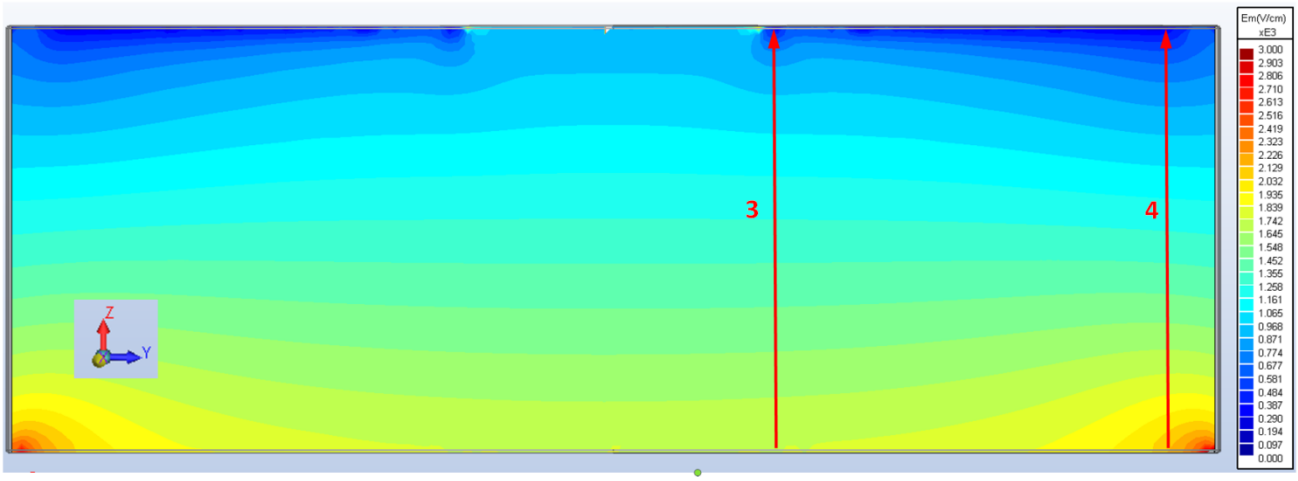

Fig 5. Cross section of the HPGe crystal through the trapezoidal segment area showing the electric field contours. The lines labeled 3 and 4 refer to the Ez field component plots in fig 7.

strength beyond that modeled here. But for purposes of proving the design concept it is sufficient to model the "worst case" lowest operating bias. Figure 5 shows a similar plot for a plane bisecting the radial gaps between the trapezoidal segments. Here the electric field is generally weaker in the gap areas, as would be expected. Finally, figure 6 shows an electric field plot in a plane parallel to the segmented electrodes at 0.1 mm below the crystal surface, specifically in the weak field gap area between the two trapezoidal electrodes. Figure 7 is a plot of the Ez component of the electric field for the four lines in the Z direction shown in figures 4 and 5. The Ez component of the field is largely responsible for sweeping the generated electrons and holes to the ion implanted electrodes and HV bias contact, respectively, and is therefore the dominant factor in determining the charge collection time. It can be seen that Ez varies from about 300 Vcm^{-1} to $2kVcm^{-1}$ depending on the Z position and the proximity to the weak field gap zones. Also shown in figure 7 is the Ex field component across the weak field area illustrated in figure 6 with values dipping to 300 Vcm^{-1} across the short distance between the electrodes. To estimate the best and worst case charge collection times in the final crystal model, the electron and hole electric field strength was modeled along each of the four charge paths shown in figures 4 and 5, and then transformed to the electron and hole drift velocity using the data in figure 1. The total drift time was calculated by integrating the time along the path in 0.01 mm steps. Using this method, the electron and hole transit time along the full length of each path are shown in table 1.

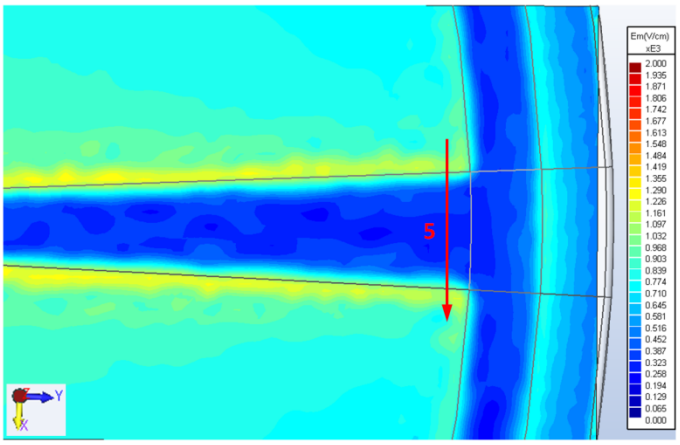

Figure 6. Electric field plot in a plane parallel to the segmented electrodes 0.1 mm below the crystal surface, showing the weak field gap area between the two trapezoidal electrodes and the guard ring. The line segment in the X direction refers to the Ex electric field component shown in figure 7.

For the center electrode, the best case transit time is 128 ns and corresponds to gamma ray absorption and charge generated close to the (negatively biased) HV electrode, the signal being formed from electron motion only (path #1). The worst case drift time for the center electrode corresponds to the case where the interaction is close to the gap zone around the outside of the center electrode, represented by path #3 in figure 5, with a hole drift time of 170 ns (table 1). Similarly, the best case drift time for the trapezoidal electrode is for gamma ray absorption near the HV and electron motion along path #2, which calculates to 128 ns, (table 1); the worst case (172 ns) is for holes moving the full distance from the outer edge of the segmented electrode area to the HV along path #4.

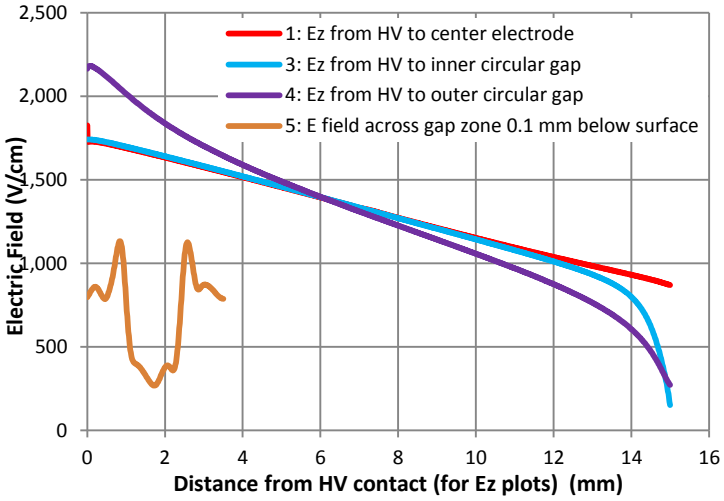

Figure 7. Ez component of Electric Field (V/cm) vs Distance from HV electrode for the paths shown in figures 4 & 5, and E field magnitude across gap zone 0.1 mm below surface as shown in figure 6.

Another consideration is the small amount of drift in the X and Y directions, especially near the weak fields in the gap zones. To check the magnitude of this effect, we calculated the electron transit time along path #5 in figure 6, (0.1 mm below the crystal surface), in the worst case of charge drifting in the weak field from the center of the gap to the edge of the electrode. The calculated time of 24 ns (table 1) is small compared to the total drift times under consideration. However, as previously mentioned, the actual electric field in the gap area of a working detector will be dependent on surface charge effects and may vary somewhat from the model. Our design mitigates this effect by restricting the gap width to 1.5 mm.

Drift path	Holes	Electrons	
HV to Center Electrode. Path 1	168 ns	128 ns	Best Case Center Electrode
HV to Trapezoidal Electrode. Path 2	168 ns	128 ns	Best Case Trapezoidal Electrode
HV to Inner circular gap. Path 3	170 ns	131 ns	Worst Case Center Electrode
HV to Outer circular gap. Path 4	172 ns	133 ns	Worst Case Trapezoidal Electrode
Across gap, 0.1 mm below surface. Path 5	-	24 ns	

Table 1. Calculated charge drift times along the paths shown in figures 4, 5, and 6

In summary, the work of Task 1 accomplished Technical Objective 1 by delivering a detector design that met the target specifications of <5pF electrode capacitance, <200 ns signal rise time, and with a detection efficiency similar to a small coaxial HPGe detector.

4. Task 2: Validation of Capacitance and Electric Field models.

The purpose of this task was to validate the results achieved in Task 1 by applying the same capacitance and electric field models, (derived from the "Coulomb" software program), to examples of existing HPGe detectors that shared some of the characteristics of the proposed innovation.

4.1 Capacitance model validation.

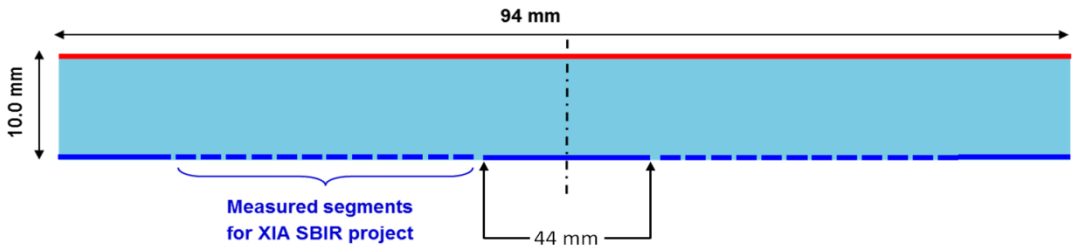

Figure 8. Cross section of the Canberra segmented planar HPGe detector used for capacitance validation.

To test and validate the capacitance model, measurements were performed on a segmented planar HPGe detector of dimensions 94 mm diameter by 10 mm thick, with a segmented electrode pattern of 12 closely spaced concentric rings (figure 8). The ring width was 1.45 mm with 0.3 mm spacing. Like the detector under development, the capacitance of each electrode to ground was highly dependent on the inter-electrode capacitances due to the small spacing, (although the actual capacitance values are an order of magnitude larger). Capacitances were measured using an impedance meter with the detector fully cold and under HV bias, but with no front-end electronics. Table 2 shows the total measured capacitance to ground for each electrode and compares the results to the XIA model. There is a small systematic disagreement between the simulated and measured capacitances that increases to about 2% at the highest values. Nevertheless, the overall agreement is very good and the error can be considered very small for purposes of the current project. We therefore concluded that the various features and operating parameters of the Coulomb modeling software program had been set up correctly and the program as functioning as designed.

	Capacitance (pF)		
Segment	Measured	XIA sim	Delta
1	44.0	43.71	-0.29
2	47.1	47.03	-0.07
3	50.2	50.42	0.22
4	53.3	53.72	0.42
5	56.4	57.05	0.65
6	59.5	60.38	0.88
7	62.6	63.71	1.11
8	65.7	67.05	1.35
9	68.8	70.39	1.59
10	71.9	73.70	1.80
11	75.0	76.99	1.99
12	78.1	80.17	2.07

Table 2. Comparison of measured and simulated electrode capacitance on the Canberra ringed planar HPGe detector. Error bars are implied by the recorded precision.

4.2 Electric Field model validation.

Attempts to use the Canberra ringed segmented HPGe to validate the electric field model and variations in charge drift times were not successful, due to the relatively long (>200 ns) intrinsic rise time from the preamplifier. For example, it was not possible to obverse any significant variation in the preamplifier rise times when a tightly collimated Am^{241} source (60 keV gamma peak) was tracked across the segmented surface of the detector. Therefore, as an alternative validation test, it was decided to model the electric field and charge drift time inside the so-called "Point Contact" coaxial detector developed by the Lawrence Berkeley National Lab [3]. The main features of this detector are the very low capacitance contact (~1pF) and relatively weak electric fields (and long charge collection times) throughout a large part of the detector volume. The latter feature makes the Point Contact detector a good candidate for testing the XIA electric field and charge drift models. The input to the model, such as the detector dimensions, operating voltage and net carrier density were provided in reference [3]. The resulting electric field distribution from the XIA model is shown in figure 9, and is essentially the same as that in the published literature. Using the technique established in Task 1, the charge drift time was calculated for holes drifting along the center axis from the negatively biased outer contact to the small point contact, (red arrow in figure 9). The calculated drift time was 810 ns, which compares to 800 ns in ref [3]. The XIA model is in very close agreement with the published data for the Point Contact detector, and therefore is assumed to be accurate for the weak field modeling of the HPGe detector under development.

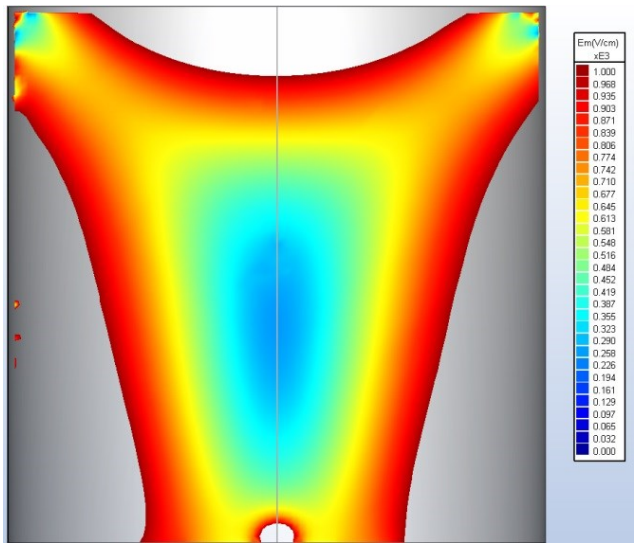

Figure 9. Cross section of Point Contact detector [3] showing electric field distribution generated by "Coulomb" software. Gray areas indicate fields in excess of 1 $keVcm^{-1}$.

In summary, Task 2 achieved technical Objective 2 by validating both the capacitance and electric field models against real-world measurements and previously published data.

5. Task 3. Detector noise model, and sources of excess noise.

The purpose of this task was to build a model to predict the noise and energy resolution characteristics of the final detector design, taking account of sources of excess noise, where possible. An understanding of the detector noise performance is a critical factor in the overall system design, as the electronic noise can strongly affect the efficacy of the detector when operating at high count rates and short processor peaking times.

5.1 Background noise theory

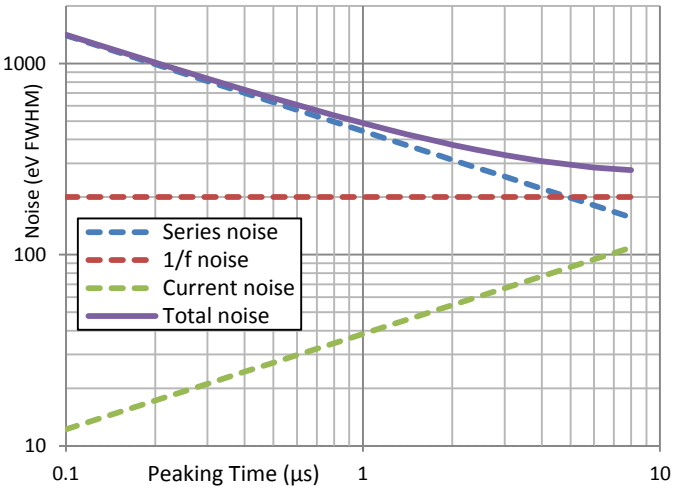

Figure 10. Theoretical noise versus peaking time for a low-capacitance HPGe detector.

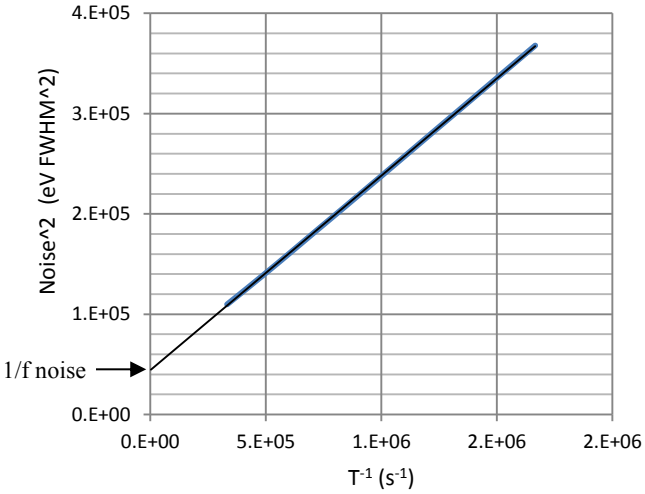

Figure 11. Plot of Noise^2 vs. T^{-1} to determine 1/f noise.

Figure 10 is a theoretical plot of noise versus peaking time from a low-capacitance HPGe detector, and shows three components that contribute to the total noise; the series (or Johnson) noise from the FET, 1/f noise, and leakage current noise. For short peaking times, (which is relevant to this project), the noise is dominated by the series component, which for most analog shaping amplifiers and digital pulse processors can be expressed by the formula in equation 1, where C is the total capacitance at the gate of the FET in pF (including the FET, detector, feedback and stray capacitance), En is the series noise of the FET expressed in nV $Hz^{-1/2}$, and T is the pulse processor peaking time in µs:

Series noise (eV FWHM) = 44.3 En C $T^{-1/2}$ ---------- Eqn. (1)

The values of En and C are determined from data supplied by the FET manufacturer and from the detector capacitance model, and both are known to better than 10% error. An investigation of the origins of 1/f noise in the FET, detector, and other front-end components are beyond the scope of the present work, but the total 1/f noise can be extracted from the type of data shown in figure 10 by plotting (noise)^2 versus T^{-1}, the intersect on the Y-axis being the square of the 1/f value. An example of such a plot is shown in figure 11, which uses the same data as figure 10. A determination of the 1/f noise value permits a more accurate extraction of the series noise from the total noise measurement. The third component, leakage current noise, should not be a concern when operating at short peaking times. For example, the current noise in figure 10 is plotted for 10pA detector leakage, and is still relatively small even at 8µs peaking time. Therefore, for a given FET type, and using a capacitor to simulate the detector capacitance, it is possible to make a reasonable comparison between the theoretical and measured noise values at different peaking times and thereby quantify any 1/f and other excess noise that should be taken into account in the final model.

5.2 Noise measurements with MX 16 FET and simulated detector capacitance.

For high rate (and low noise) applications it is desirable to use an FET with a built-in Reset transistor in place of the feedback resistor, since the resistor adds noise and sets a limit on the input count rate determined by the DC offset at the preamp output. Commercially available Reset type FETs are most commonly supplied by Moxtek at a cost of about $300 each. According to the Moxtek data sheet, the FET model MX16 is a particularly good match (in terms of capacitance and noise) for a detector capacitance in the 4-5 pF range. Other FET options were investigated such as the low-cost BF862 mounted with an external Reset transistor. The BF862 was found to work satisfactorily with respect to signal rise time and Reset function, but the noise at short peaking times was about a factor of 2 worse than the MX16. The $300 price for the Moxtek device is relatively low compared to the total system cost, and given its superior noise performance it was decided not to pursue the BF862 option beyond some initial measurements.

Two MX16 FETs were purchased for our tests, one in a standard TO72 can, and one in a low Teflon package designed to reduce dielectric (1/f) noise. To avoid duplication, only the results from the Teflon packaged FET are presented here. The operating parameters and specifications of the MX16 are shown in Table 3.

	Vd	Id	Vsub	Temp	Capacitance	Noise
Moxtek data sheet	4 V	5 mA	Vgs ~0V	170K	4 pF	0.6 nV $Hz^{-1/2}$
Actual operating point	3.1V	2 mA	Vgs~0V	130K	4 pF	Assumed 0.65 nV $Hz^{-1/2}$, but exact value unknown.

Table 3. MX16 operating parameters and specifications

Figure 12 is a photograph of the MX16 FET package with connecting wires and components mounted inside a liquid nitrogen (LN) cooled test cryostat, (with the cryostat end-cap removed). When cooled, the FET operating temperature was about130 K. The corresponding schematic of the test circuit is shown in figure 13. The detector was simulated with a 5pF capacitor, which also functioned as the input for the test pulser. A feedback capacitor with nominal value 0.5 pF was chosen to permit a maximum energy range of a few MeV. A small (<1V) negative bias was applied to the gate of the FET through a 10G Ohm resistor to simulate the detector leakage current and generate the saw-toothed Reset type signal at the output pf the preamp.

The test circuit was calibrated by first assuming the value of the simulated detector capacitance (5.0 pF), and then accurately measuring the feedback capacitor from the signal gain of the pulser. Once the feedback capacitor value was known, (in this case 0.54 pF), the equivalent gamma-ray energy in an HPGe detector (i.e. charge on the feedback capacitor) was easily calculated for a given pulser amplitude. The pulser level was

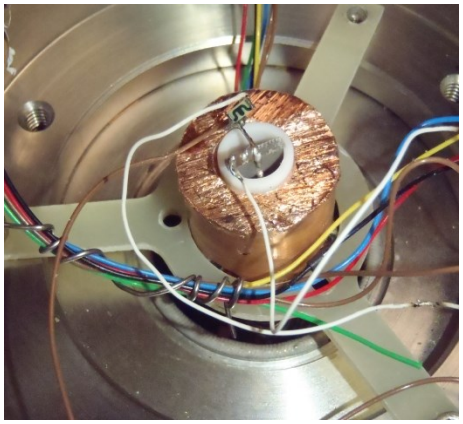

Fig 12. Photograph of MX16 FET package mounted inside the test cryostat.

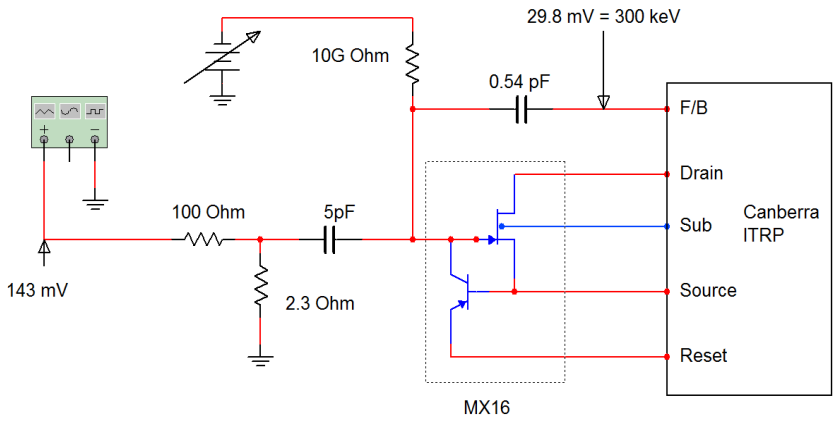

Fig 13. Schematic of test circuit used for noise measurements

chosen to correspond to an energy of 300 keV, and the eV FWHM noise was measured by the resulting pulser width on a calibrated energy spectrum. The most significant error in the energy calibration (and hence noise measurement) was the assumed value of the simulated detector capacitance, given the potential for various stray capacitances. Assigning an error of ± 10% to the noise measurement is a reasonable assumption.

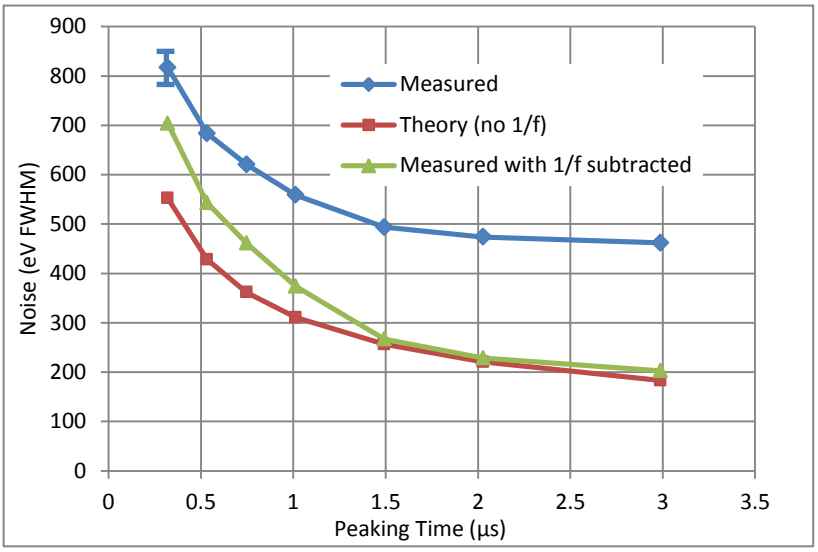

Fig 14. Comparison of measured and theoretical noise vs. processor peaking time for test set up in figs 12 and 13. The first point of the measured data shows the magnitude of the potential systematic measurement error.

Figure 14 shows the result of the noise measurements using the test set-up in figures 12 and 13, compared to calculated values from equation (1). An additional 1pF stray capacitance to ground was added for the calculated number, which is a typical value in a real-life cryostat assembly. There are two notable features of the data in figure 14: Firstly, there is a large (> 400 eV FWHM) 1/f noise component, the source of which could not be readily identified. Possible sources include noise from the pulser itself, the 10G Ohm bias resistor, or the 5pF "detector" capacitor, although any excess noise from these components is expected to be much less than the magnitude observed. Therefore, the excess 1/f noise will be investigated further in the early stages of Phase II.

The second feature of the data in figure 14 is the increase in measured noise at short peaking times compared to theory, (green and red lines). This could be due to the suboptimal setting of the FET operating parameters, (see table 3), or some source of high frequency pick-up from a ground loop. Regarding the FET settings, it was necessary to reduce the drain current to a 2 mA, compared to the Moxtek test condition of 5 mA, in order to stop the preamp circuit from oscillating. The cause of the oscillation, to be investigated further in Phase II, is believed to be the inductance in the long (>10 cm) drain wire to the FET, which adds an additional phase lag at high frequencies and induces oscillation. (In the completed detector design, the FET wires are expected to be up to 30 cm long to accommodate mounting of the 22 preamplifiers.) The reduced drain current increases the series noise of the FET beyond that expected from the data sheet, although unfortunately the expected noise figure at 2 mA is unknown.

The conclusion from this section of work is that a worst-case noise value of 800 eV FWHM could be expected at 0.3µs peaking time, which is the most likely operating point for very high rate data collection. Furthermore we can conclude that the noise may be reduced towards 550 eV FWHM with a redesign of the preamplifier circuit (to stop oscillation), full optimization of the FET operating conditions, and with a better understanding of the source(s) of 1/f noise in the test measurement.

5.3 Noise measurements with low capacitance HPGe planar detector.

Additional noise measurements were performed on a small (0.85 pF) Canberra HPGe X-ray detector mounted with an FET with the same characteristics as the Moxtek MX20 device. The purpose was to check the XIA noise model against a real-world low-capacitance detector, especially to quantify the level of 1/f noise and to check for other sources of noise (such as contact resistance) that may need to be taken into account in the final model. The MX20 is a lower capacitance (but higher noise) FET compared to the MX16, and is usually used for low capacitance X-ray detectors. But nevertheless, it is an appropriate tool for checking the model under low noise conditions. The MX20 performance characteristics applied to the noise model were taken from the Moxtek data sheet. Figure 15 shows the resulting comparison of measured and calculated noise; in this case the theoretical curve includes 1pF stray capacitance on the FET gate, and the addition of 56 eV FWHM 1/f noise derived from the measured results.

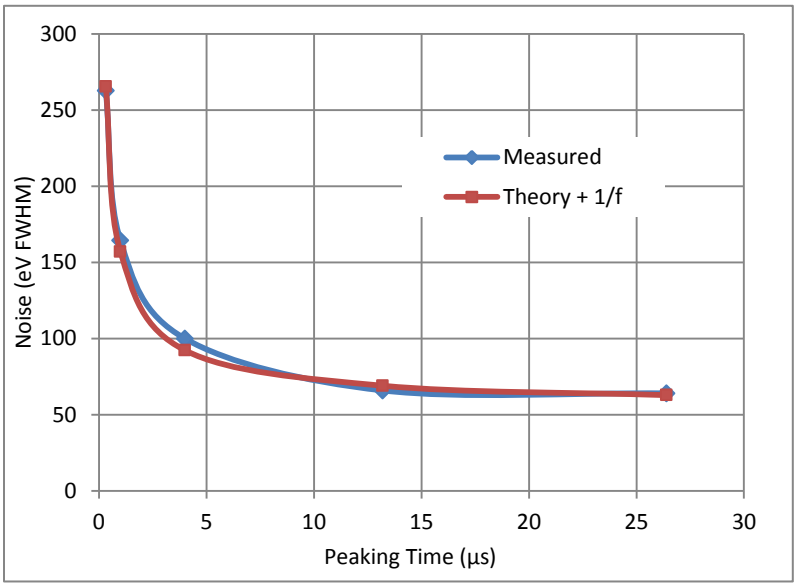

Fig 15. Comparison of measured and calculated noise vs. processor peaking time for a small (0.85pF) Canberra HPGe planar X-ray detector.

A number of conclusions can be drawn from figure 15: Firstly, the addition of 1pF stray capacitance causes a good match between measured and calculated data at short peaking times, and this value should be used in the final noise model. Secondly, the level of 1/f noise is very low in this real-world detector, and thirdly there is no evidence of additional series noise from contact resistance. This last conclusion is most probably due to the wire bonding technique employed by Canberra for connecting the FET gate to the HPGe crystal contact. Wire bonding directly to the germanium surface avoids contact resistance problems sometimes experienced by other detector manufactures; this method will be used in the Phase II detector fabrication.

5.4 Comparison of noise in a low capacitance HPGe Point Contact coaxial detector.

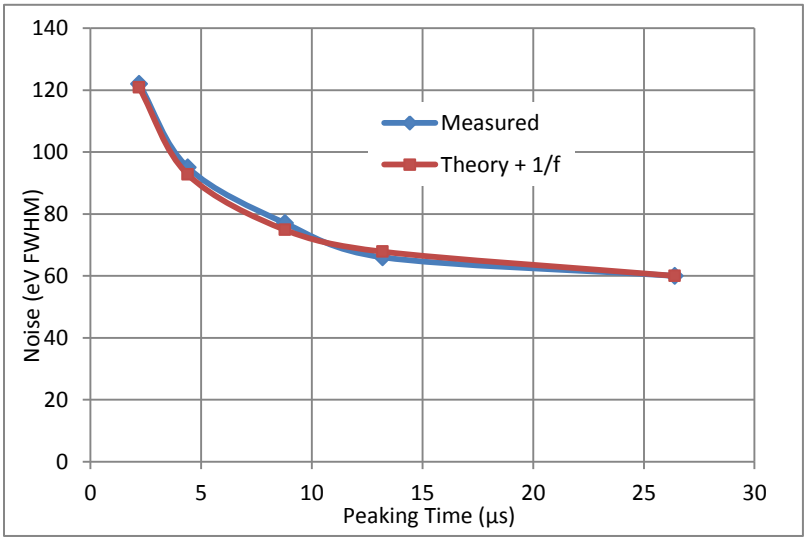

Fig 16. Comparison of measured [4] and calculated noise from the XIA noise model vs. processor peaking time for a low capacitance (1pF) Point Contact coax detector.

Another comparison of calculated and measured noise was performed using published noise data from a Canberra Point Contact detector similar to the one modeled in Task 2 [4]. Figure 16 shows the comparison with the XIA noise model using the MX20 FET and assuming 1pF stray capacitance, as before. A feature of the Point Contact detector is the low capacitance (1 pF) contact in the presence of a large active volume of germanium (~180 cm^3). This is a characteristic shared by the multi-contact detector under development, and it is therefore encouraging to observe that the 1/f noise component in figure 16 is very low, (about 51 eV FWHM), implying that the 1/f noise in the multi-contact detector could be much lower than that observed in the experimental data of figure 14.

5.5 Noise contribution from multiple contacts

When the charge from a single gamma-ray event is collected by more than one electrode, the noise in the summed signal is increased compared to a single electrode event. Consider the case illustrated in figure 17, which represents the preamp signals from a single gamma-ray event collected simultaneously on three different electrodes. E_i is the energy deposited on electrode i, and N_i is some representation of the signal noise for that electrode, such as eV FWHM. For each electrode, N_i is the quadrature summation of the electronic noise (N_0, assumed to be the same for all electrodes) and the energy-dependent statistical variation in the signal (F_i), sometimes referred to as the "Fano noise"; equation (2). The magnitude of F_i is determined only by the

properties of the detector material, (in this case germanium), and the deposited energy, E_i, as expressed in equation (3) for germanium.

$$N_i = (N_0^2 + F_i^2)^{1/2} \quad \text{---------- Eqn. (2)}$$

$$\text{where } F_i \text{ (eV FWHM)} = 1.30*E_i^{1/2} \text{ } (E_i \text{ in eV}) \quad \text{---------- Eqn. (3)}$$

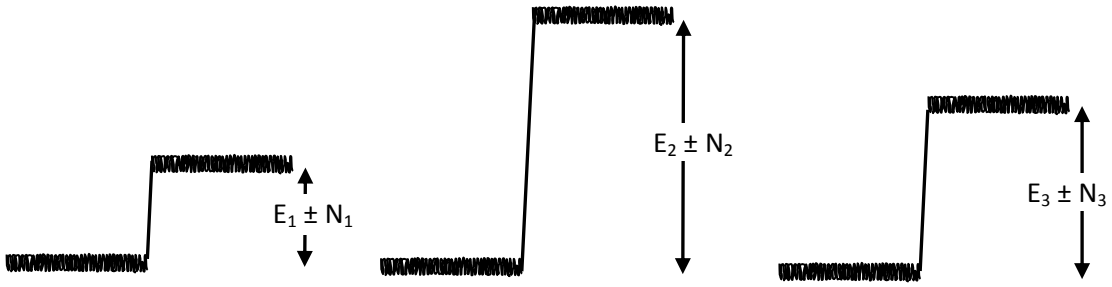

Figure 17. Representation of preamp signals from a single gamma-ray event collected by three different electrodes, with deposited energy E_i and noise level N_i.

It is important to note in equation (3) that the "Fano noise" components, F_1, F_2 and F_3, for our 3-electrode example are correlated sources of noise. That is, in the case of a 662 keV gamma-ray fully absorbed in the detector and fully collected by only the three electrodes, the sum of F_1, F_2 and F_3 must always be 1060 eV FWHM, (from equation (3)). Therefore, using equations (2) and (3) for an absorbed energy E (eV), the total noise N_T on the summed signal from three electrodes becomes

$$N_T = [3N_0^2 + F_1^2 + F_2^2 + F_3^2]^{1/2} = (3N_0^2 + 1.69E)^{1/2} \quad \text{---------- Eqn. (4)}$$

N_0 is the electronic noise from a single electrode, and it is clear from equation (4) that the effective electronic noise is increased by the square-root of the number of electrodes involved in a gamma-ray event. This is an important conclusion and affects the noise performance of the system as a whole. In order to estimate the magnitude of this effect, a Monte Carlo simulation was performed on the two-crystal detector assembly design to determine the average number of Compton scattered events for a fully absorbed 662 keV photon. The simulation showed this number to be 4 at 662 keV. In addition, a rough calculation was performed to estimate the probability of charge sharing between two electrodes from a single interaction point in the detector, based on the relative surface area of the low-field gaps between the electrodes. The result increased the average number of signal electrodes by a factor 1.16. However, there is also a probability that charge generated by different Compton scattered events is collected on the same electrode, which will reduce the average number of electrodes involved per event. This will be studied more fully in Phase II, as will the energy dependence (from Compton scattering) of the "noise multiplication factor", as well as other effects such as charge diffusion. Finally, it should be noted that other energy summation schemes are possible that will mitigate the noise effect of multiple electrodes; it is feasible to collect spectrum data only from events that trigger one, or two, or three electrodes, for example, rejecting the (noisy) high order multiple electrode events. The result will be improved energy resolution, but with an increase in Compton background. The optimum configuration for summing the electrode signals will be studied both theoretically and empirically in Phase II. But for purposes of the Phase I feasibility study it is sufficient to assume 4 electrodes are involved for each fully absorbed 662 keV gamma-ray, which increases the electronic noise by a factor of two at 662 keV compared to the single-electrode calculation.

5.6 Signal Rise Time and Reset function with MX16 FET.

The circuit shown in figure 13 was used to check that the MX16 FET (operating with the Canberra ITRP preamp) was capable of an intrinsic rise time of 100 ns or less, so that the front-end electronics is not adding significantly to the signal timing resolution.

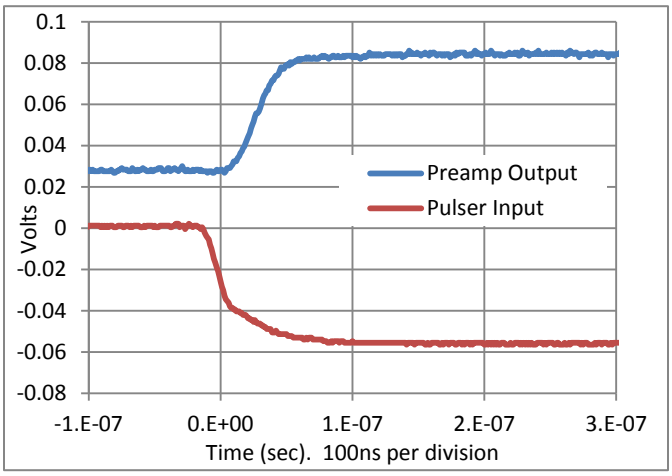

Fig. 18. Signal response of MX16 FET (at 130K) and Canberra preamp with 5pF simulated detector load and 0.5 pF feedback.

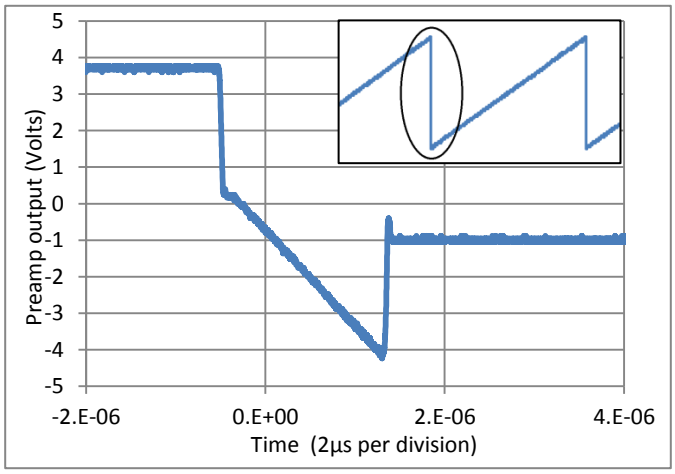

Fig 19. Response of Reset function using the Canberra ITRP preamp and MX16 FET, using the circuit in figure 13.

Figure 18 is the response to a fast-rising (50 ns) pulser signal, and it can be see that the 0-100% preamp output is significantly less than 100 ns.

The duration of the Reset period is another important characteristic of the FET and preamp combination, as a long Reset duration will add to the overall dead-time of the system. For example, with a 0.5pF feedback capacitor the preamp will reset approximately every 70µs with 1 Mcps input at 662 keV energy. Therefore the Reset period should be no longer than a few microseconds to avoid adding significant dead-time. Figure 19 shows the Reset period to be approximately 2µs, which is satisfactory.

5.7 Crosstalk noise between segmented electrodes.

Crosstalk occurs when the signal forming on one electrode induces a (smaller) corresponding signal on an adjacent electrode, usually by capacitive coupling. The effect is to add unwanted low energy peaks in the spectrum that can interfere with the genuine data. Crosstalk can occur from either high energy gamma-ray events or (more significantly) from the Reset signal of a neighboring electrode. All multi-element detectors are prone to crosstalk noise, particularly in the case of segmented electrodes with relatively high (~1pF) inter-electrode capacitance. Therefore a circuit simulation was performed (using the program Multisim from National Instruments) to estimate the effect of crosstalk in the detector under development, where the inter-electrode capacitance is 1.1 pF. The simulation injected a large signal into the input of one FET and preamplifier (with appropriate detector load and feedback) and measured the output on a second FET/preamplifer circuit coupled to the first through 1.1pF between the FET gates. The result is shown in figure 20, where it can be seen that the induced crosstalk signal is approximately 1% of the original magnitude.

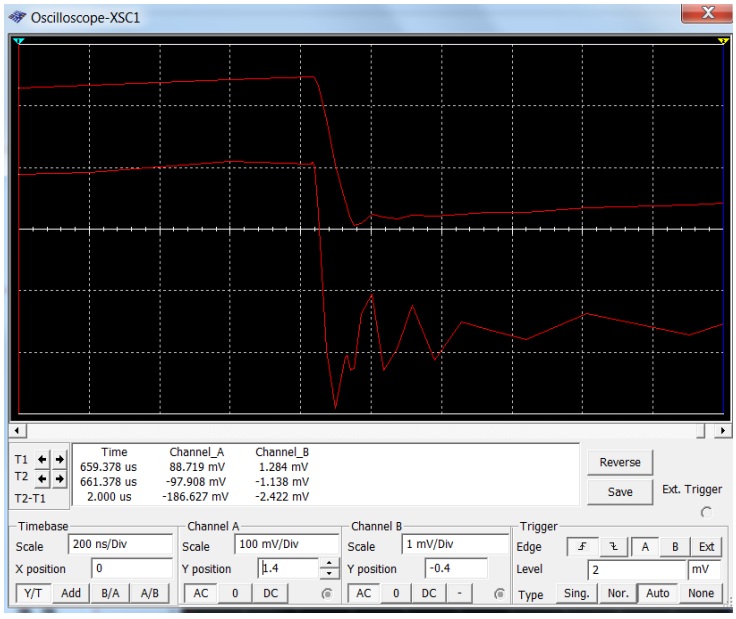

Figure 20. Simulated effect of cross talk from a large Gamma pulse: Upper trace = main preamp signal. Lower trace =cross-talk signal on adjacent segment: Note change of scale: 1/100 reduction in amplitude.

Using this simulation as a guide, a 10 MeV gamma-ray will induce a crosstalk signal of 100 keV, which is at the lower limit of the energy

range of interest for nuclear safeguard applications. However, referring to figure 19, a 3V positive-going step from the Reset signal corresponds to an equivalent energy of 30 MeV. In this case, the 1% crosstalk signal is 300 keV, which may encroach on peaks of interest. There are methods to remove Reset crosstalk by the use of a logic inhibit signal during the Reset period, but to work effectively, either all channels must Reset simultaneously, (which is difficult to implement), or the inhibit signals from all channels must be joined together in a logical "OR", which can add significantly to the total Reset dead-time. The magnitude of crosstalk and possible solutions are worthy of further study in Phase II.

5.8 Total Noise model.

Using equation (1) and the results of Task 3, figure 21(a) is the calculated worst-case noise and 662 keV energy resolution as a function of pulse processor peaking time. The blue line is the single-electrode noise, and the red line shows the effect of the noise multiplication factor (at 662 keV) after summing the signal from multiple electrodes. The green line is the resulting 662 keV energy resolution with the multiple-electrode noise added. The value of the 1/f noise in figure 21(a) is 400 eV FWHM, taken from the measured noise data in figure 14.

There is a realistic expectation that the 1/f noise in the detector under development will be much less than 400 eV FWHM, given the values measured (50 eV FWHM) in existing low capacitance HPGe detectors, (figures 15 and 16). Therefore, in figure 21(b) the noise and energy resolution has been recalculated with a conservative estimate of 200 eV FWHM 1/f noise, to show a reasonable prediction of the noise performance at 662 keV in the finished detector. As mentioned in section 5.5, a study of the noise as a function of energy will be conducted in Phase II, taking account of the energy-dependent noise multiplication factor and charge diffusion; a refined noise model will be an important aid to validating the performance of the completed detector system.

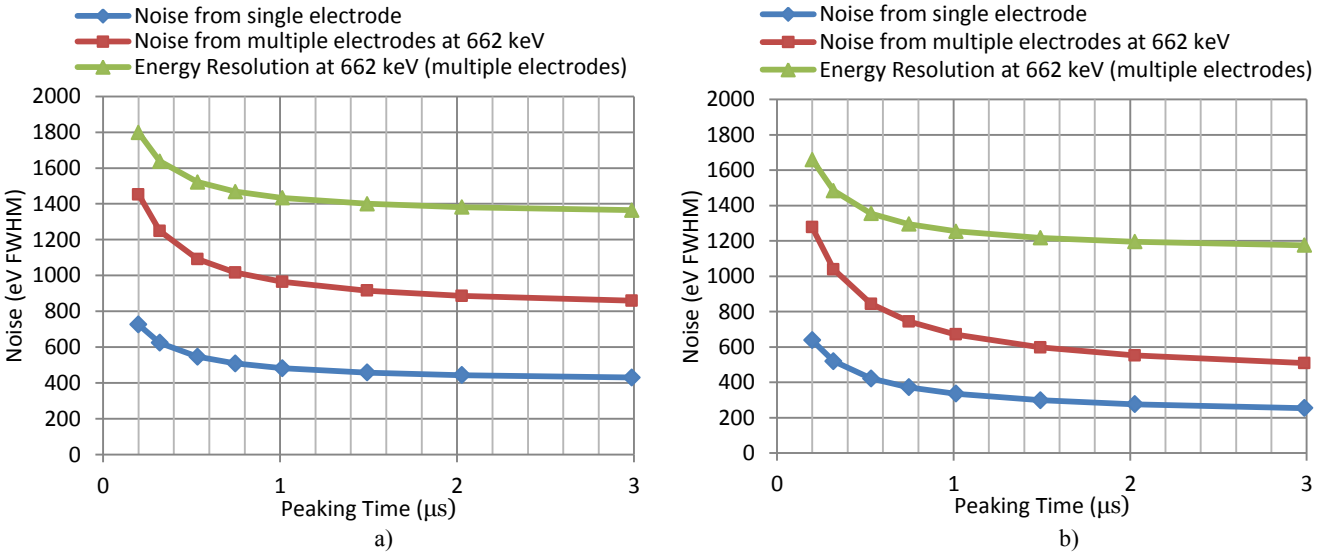

Figure 21. Predicted noise and energy resolution vs. Peaking Time for 22-channel detector. a) 1/f noise = 400 eV FWHM. b) 1/f noise = 200 eV FWHM

5.9 Task 3 Summary

In summary, the following conclusions can be drawn from the work of Task 3:

- The MX16 FET is a good choice for the detector under development with respect to series noise, signal rise time, and Reset function.
- Some preamplifier redesign is needed to optimize the performance with the MX16, especially with long drain wires. (Phase II task).

- Noise measurements with the MX16 and simulated detector capacitor showed a high level of 1/f noise that was not present with real-world low-capacitance detector measurements with the MX20 FET. This remains an open issue to be investigated in Phase II.
- Contact resistance is not likely to be an issue in the Canberra detector, based on results from previously fabricated low capacitance and low noise detectors.
- Increased noise from summing the signal from multiple electrodes is significant. An initial estimate of this effect has been made, but will be explored more fully in Phase II.
- Crosstalk from Reset signals may interfere with the spectrum at the lower levels of the energy range of interest, and may need to be removed using logic inhibit signals.
- Task 3 fulfills Technical Objectives 3 and 4, except that the magnitude of 1/f noise is an open issue at the end of Phase I.

6. Task 4: Crystal housing and cryostat design

The crystal housing and LN cryostat assembly was developed with the 3D modeling software SolidWorks, taking account of the following design factors:

- Crystal mounting: Rigid support with good thermal path, but sensitive (passivated) areas of the detector not touched.
- Thermal conductivity path and losses.
- Mounting and bonding of FET and feedback components.
- Vacuum integrity: Materials, trapped holes, and surface emissivity.
- External mounting of preamplifiers.

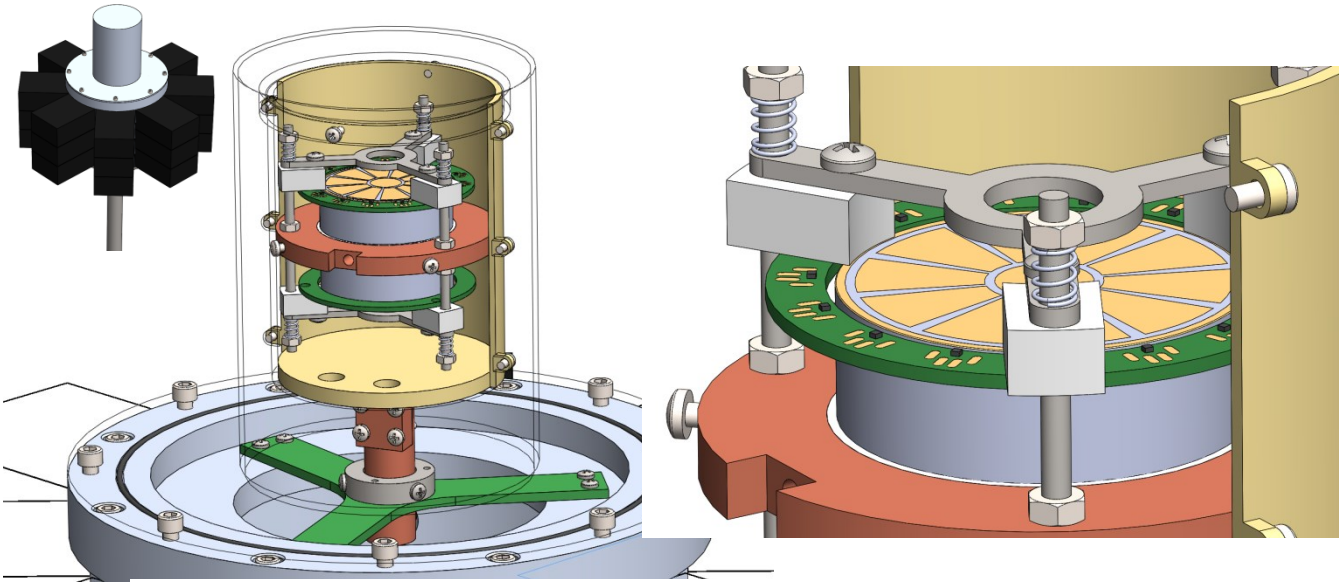

Figure 22. Cutaway drawing and close up of the crystal housing and LN cryostat. (Wiring not shown)

6.1 Cryostat Description

Figure 22 is a cutaway illustration and close up of the completed design, showing the two back-to-back HPGe crystals mounted in the LN cryostat with FET and feedback components. Each crystal is seated in a thin-walled Teflon insulating cup inserted on one side of a 6 mm thick aluminum plate, (brown color in figure 22), which is recessed by 2mm on each side to hold the Teflon cups. The HV contact is made through an indium pad between the crystal face (n^+ contact) and the Teflon, with the HV wires running through a radial hole in the aluminum. The crystals are secured by spring pressure through three insulating blocks (Delran or similar material) that contact only the guard ring area. The FETs (just visible as small black cubes in figure 22) and feedback

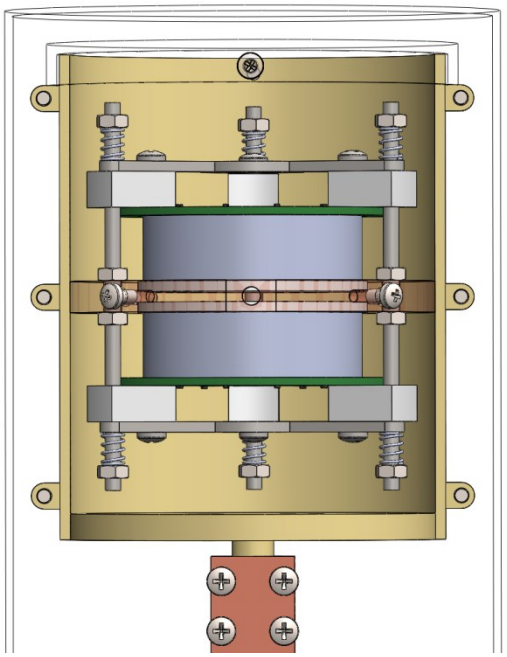

Figure 23. View of the inner HPGe crystal mounts and inner cup. (The copper supporting plate is shown semi-transparent).

components are mounted on a low-loss circular printed circuit board (PCB) in the same plane as the crystal surface. The FET gate wires are bonded directly to the segmented electrodes, thereby eliminating contact resistance noise. One possible design issue is the relatively long (>20 mm) bond wire required for the detector center contact, and the potential for microphonic nose; the magnitude of microphonic noise will be studied in Phase II. The other FET connecting wires are routed from the PCB bond pads through holes in the inner cup to the vacuum feed-throughs and external preamplifiers.

Figure 23 is another view of the mounted crystals with the aluminum plate displayed as semi-transparent. The plate is screwed to the inside of the inner cup, which provides both an enclosed volume for infrared shielding and the thermal conduction path from the cold finger. Note that the plate is potentially a source of gamma radiation shielding for the HPGe crystals. However, a linear absorption calculation shows that the transmission is greater than 75% for 662 keV gamma-rays traveling radially through the maximum thickness of the aluminum. The inner cup is also fabricated from aluminum, and is coated with nickel and gold to improve the surface emissivity. The cold finger is of a standard construction for HPGe detectors, the upper part being held in place by an insulating support, with a short section of copper braid in the conduction path to mitigate vibrations and microphonic noise.

The cryostat end-cap outside diameter is 3.75", which is a standard size for HPGe detectors. The small inset in figure 22 illustrates the current design for mounting the (relatively large) Canberra ITRP preamplifiers in stacks of three, using a separate aluminum block, which is bolted and vacuum sealed to the bottom of the cryostat end-cap flange. A Phase II task is to redesign the preamplifier with the likelihood of a smaller footprint. In this event, the preamp mounting block can easily be changed to accommodate new designs without affecting the internal components.

6.2 Thermal calculation.

There are three main sources of heat load to be taken into account when estimating the crystal operating temperature:

1. Thermal radiation losses from the inner cup to the cryostat end-cap, which is at room temperature.
2. Conduction losses through the FET wires to the (room temperature) vacuum feed-throughs.
3. Heat generated by the 22 internally mounted FETs.

For large differences in temperature, thermal radiation losses for a cylinder of radius a and length L can be calculated from equation (5), where E is the emissivity coefficient of the material, σ is Stefan's constant, and T_r is room temperature.

$$\text{Radiation loss (Watts)} = 2\pi.a.E.\sigma.T_r^4.L \qquad \text{---------- Eqn (5)}$$

The radiation loss calculates to 0.25 W when using the dimensions of the inner cup and the emissivity of polished gold. However, the gold plated surface of the inner cup will likely not have the theoretical emissivity coefficient of 0.025. For comparison, the emissivity of aluminized Mylar is 0.08, which results in 0.8 W of thermal power. Therefore, to account for the non-ideal emissivity of the gold plating, we will assume a radiation loss of 0.5 W in the present calculation.

The FETs are connected to the preamplifiers by a total of 88 wires, (4 wires each). Due to the positioning of the preamplifiers the average length of the wires is quite long; we will assume 32 gauge copper wire of 30 cm length. Based on a simple thermal conductance calculation, the total heat load from the wires is 0.54 W. If necessary, the heat losses from the FET wires can be reduced by the use of Kovar pins at the vacuum feed-throughs to break the thermal conduction path.

The drain of each FET will be operated at about 3V and 5mA, resulting in an additional 0.33 W heat load. The total thermal power therefore equates to 1.37 W, which will be rounded up to 1.5 W for purposes of calculating the detector operating temperature. Note that a standard, small volume HPGe coaxial detector is usually assumed to generate 1W heat load, resulting in the consumption of about 0.5 L of LN per day (ignoring other losses in the Dewar). So the calculated value for the multi-contact detector is consistent with past experience.

With the heat load established, a simple conductivity calculation was performed for the thermal path from the cryostat cold finger (assumed to be at 80K) to the HPGe crystals. A total temperature drop of 9K was calculated, resulting in a detector operating temperature of about 90K, which is in the acceptable range for an HPGe detector. Although this calculation is sufficient to prove the feasibility of the design concept, a more detailed computer-aided thermal model will be developed in Phase II to confirm the detector operating temperature before fabricating the detector.

In summary, Task 4 has met Technical Objective #5 by developing the crystal housing and cryostat design.

7. Task 5. Response to a ^{137}Cs source.

Task 5 modeled the response of the multi-contact detector to a ^{137}Cs source for the purpose of calculating the collection efficiency at 662 keV, and for measuring the peak height to Compton background ratio at this energy. Both of these detector characteristics affect the efficacy of the instrument for detecting small peaks of interest in the presence of a large background from ^{137}Cs.

The detector was simulated using Geant4 version 4.9.4 [5], [6]. The detector was divided into five distinct regions: two representing the upper and lower active germanium volumes; two the upper and lower germanium guard rings and one the copper spacer. In these simulations photons are propagated and tracked until they either leave the world volume or are absorbed. The energy deposited via Compton scattering or photoelectric absorption in each of the two active volumes was tallied and summed on an event-by-event basis. Energy deposited in the guard rings or copper spacer is automatically accounted for. The resulting data files were analyzed in the ROOT framework [7]. Histograms were constructed from the ideal detector response function convolved with a noise model to match the expected noise properties of the detector, (see section 5.8).

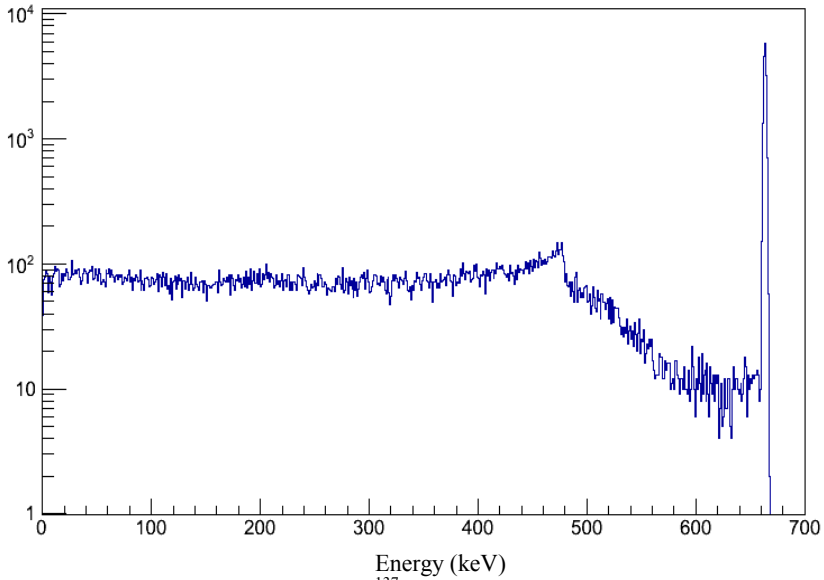

Figure 24. Geant4 simulation of a ^{137}Cs spectrum using the multi-contact HPGe detector. Pulse processor peaking time is 0.3μs

Figure 24 shows the resulting simulated ^{137}Cs spectrum with an electronic noise value taken from figure 22(b) at 0.3μs processor peaking time. The simulation used a point source emitting 662 keV photons isotropically distributed at a distance of 25 cm from the detector end-cap. The ratio of the 662 keV peak

integral to total events in the spectrum is 15.8%, and the ratio of the 662 keV peak height to the background just below the Compton edge is about 60:1. An absolute efficiency was computed for the same conditions, and a value of 0.018% was obtained by the number of counts under the 662 keV full energy peak divided by the total number of events. Confidence in the result was strengthened by repeating this simulation with 10 keV photons, each of which undergoes photoelectric absorption; the absolute efficiency derived in this run closely approximates that from a straightforward analytical computation.

For completeness, the simulation was repeated with 1332 keV (^{60}Co) photons. In this case, the absolute efficiency was 0.0093%, which equates to an IEEE Standard relative efficiency for a coaxial detector of 7.75%.

The work in Task 5 completed Technical Objective #6.

8. Task 6. Reporting

Internal reporting to XIA management and technical staff has continued throughout the course of Phase I. A poster displaying interim project results was presented at the University & Industry Technical Interchange (UITI) review meeting in Walnut Creek, CA in June 2014. A phase II proposal has been written and submitted.

9. Summary

The Phase I effort has delivered a multi-contact HPGe detector design that meets the target specifications for high count rate and high resolution performance. The feasibility of the design has been proven with respect to low capacitance contacts, electronics noise, charge collection time, front-end electronics, the cryostat housing and detector operating temperature, and the spectrum response to a ^{137}Cs source. Furthermore, XIA has fostered collaboration with Canberra to fabricate the detector and cryostat in Phase II and to eventually market and sell the commercial instrument. During Phase I, both XIA and Canberra made significant in-kind contributions related to the testing of existing HPGe detectors and other work.

With the Phase I work completed, the project is poised for the fabrication and testing of the detector and high-rate electronics in Phase II.

10. References

[1] L. Reggiani, C. Canali, F. Nava, and G. Ottaviani, “Hole drift velocity in germanium”, Phys. Rev. B Vol 16(6), (1977).

[2] C. Jacoboni, F. Nava, C. Canali, and G. Ottaviani, “Electron drift velocity and diffusivity in germanium,” Phys. Rev. B Vol 24(2), 1014–1026 (1981).

[3] P.N. Luke, F.S. Goulding, N.W. Madden and R.H. Pehl, “Low capacitance large volume shaped-field germanium detector”, IEEE Trans. Nucl. Sci. Vol 36(1), 1989.

[4] V. Marian, B. Pirard, P. Wendling, P. Quirin, M.O. Lampert, “Novel Ultra-low Electronic Noise HPGe Detector Structure for Record Energy Resolutions”, presented at the 2014 Symposium on Radiation Measurements and Applications (SORMA XV), Ann Arbor, Michigan, USA.

[5] S. Agostinelli et al., “Geant4 - a simulation toolkit”, Nucl. Instrum. Meth. A, Vol. 506, no. 3, pp. 250-303, 2003.

[6] J. Allison et al., “Geant4 developments and applications”, IEEE Trans. Nucl. Sci. Vol 53(1), pp 270-278, 2006

[7] R. Brun and F. Rademakers, “ROOT - An Object Oriented Data Analysis Framework”, Nucl. Instrum. Meth. A Vol 389 pp 81-86, 1997.